AGU ADVANCING EARTH AND SPACE SCIENCES

JGR Space Physics

Key Points:
- An updated model of the equatorward extent of >43 keV electron precipitation has been improved by successfully removing the solar cycle bias
- Including both the Dst* and the Ring Current index reduces the error estimate to ±1.8° Corrected Geomagnetic Latitude (CGMLat) over a full solar cycle (2004–2014)
- The model is extended to the Southern Hemisphere with an error estimate of ±1.98° CGMLat

Correspondence to:
E. M. Babu,
Eldho.Babu@uib.no

An Updated Geomagnetic Index-Based Model for Determining the Latitudinal Extent of Energetic Electron Precipitation

E. M. Babu[1] , H. Nesse[1], S. M. Hatch[1] , N. Olsen[2] , J. A. Salice[1] , and I. G. Richardson[3,4]

[1]Department of Physics and Technology, Birkeland Centre for Space Science, University of Bergen, Bergen, Norway, [2]DTU Space, Kongens Lyngby, Denmark, [3]Heliophysics Science Division, NASA Goddard Space Flight Center, Greenbelt, MD, USA, [4]Department of Astronomy, University of Maryland, College Park, MD, USA

Abstract Energetic Electron Precipitation (EEP) from the Earth's plasma sheet and the radiation belts is an important feature of atmospheric dynamics through their destruction of ozone in the lower thermosphere and mesosphere. Therefore, understanding the magnitude of the atmospheric impact of the Sun-Earth interaction requires a comprehensive understanding of the intensity and location of EEP. This study improves the accuracy of a previous pressure-corrected Dst model that predicts the equatorward extent of >43, >114, and >292 keV EEP using the measurements from the Medium Energy Proton Electron Detector detector of six National Oceanic and Atmospheric Administration/Polar Orbiting Environmental Satellites and EUMETSAT/METOP satellites. The improvement is achieved through multiple linear regression of pressure-corrected Dst and pressure-corrected Ring Current (RC) indices. The RC index mitigates the baseline variation of the Dst index that created an inherent solar cycle bias in the previous model. The new model is then extended to the Southern Hemisphere (SH) after removing the South Atlantic Anomaly longitudes from the data. More than 80% of the residuals lie within ±1.8° Corrected Geomagnetic Latitude (CGMLat) in the Northern Hemisphere and within ±1.98° CGMLat in the SH.

Plain Language Summary This study aims to construct a model that predicts the geographic extent of Energetic Electron Precipitation (EEP) from the Earth's radiation belts using measurements from the Medium Energy Proton Electron Detector detector of six National Oceanic and Atmospheric Administration/ Polar Orbiting Environmental Satellites and EUMETSAT/METOP satellites. The study enhances the accuracy of the previous pressure-corrected Dst model. This improvement is implemented using multiple linear regression of pressure-corrected Dst and pressure-corrected Ring Current (RC) indices. Additionally, the study extends the model to the Southern Hemisphere after removing the South Atlantic Anomaly longitudes from the data. The result resolves the solar cycle bias that existed in the previous study.

1. Introduction

Energetic Electron Precipitation (EEP) has been a topic of increased attention in recent years due to its effect on atmospheric chemistry. Medium-Energy Electrons (MEE) precipitating from the radiation belt with characteristic energies of ≥ 30 keV, will deposit their bulk energy in the mesosphere (Fang et al., 2008; Turunen et al., 2009). The associated ionization increases the production of odd Nitrogen (NOx: N, NO, NO_2) and odd Hydrogen (HOx: H, OH, HO_2). The relatively long lifespan of NOx during polar winter allows NOx to be transported downward to stratospheric altitudes and participate in catalytic ozone destruction (Damiani et al., 2016; Maliniemi et al., 2021; Sinnhuber et al., 2012; Solomon et al., 1982). HOx is relatively short-lived but depletes ozone at mesospheric altitudes (Andersson et al., 2012; Verronen et al., 2011; Zawedde et al., 2019; Zúñiga López et al., 2022). These processes have been linked to surface climate variability through their impact on atmospheric temperature, and dynamics (Baumgaertner et al., 2011; Maliniemi et al., 2019; Seppälä et al., 2009). As such, MEE precipitation is now considered a potentially important element of the natural forcing on the upper atmosphere and potentially the climate system (Matthes et al., 2017). Therefore, understanding MEE precipitation intensity and its latitudinal extent are important in quantifying the contribution of the Sun to the Earth's climate.

In the High Energy Particle Precipitation in the Atmosphere (HEPPA) intercomparison project, Nesse Tyssøy et al. (2022) compared eight different MEE precipitation estimates based on measurements of Medium Energy Proton Electron Detector (MEPED) onboard the National Oceanic and Atmospheric Administration (NOAA) Polar Orbiting Environmental Satellites (POES) and European Space Agency's Meteorological Operational

(MetOp) Satellites. This project revealed a large uncertainty in both the intensity and the latitudinal extent of the precipitation region. In the solar forcing recommended for Coupled Model Intercomparison Project (CMIP) 6 (v3.2) (Matthes et al., 2017), the MEE precipitation is parameterized by Ap (van de Kamp et al., 2016). They apply O'Brien and Moldwin (2003)'s plasmapause model to determine the equatorward boundary of the MEE precipitation region. The Atmospheric Ionization Module Osnabrück applies 8 years of data to create a statistical representation of the precipitation region scaled by Kp. However, using the Bounce Loss Cone (BLC) estimate based on both the 0°and 90°telescope on MEPED (Nesse Tyssøy et al., 2016), Babu et al. (2022) finds that the pressure-corrected Dst index (Dst*) is the best predictor of the equatorward extent of precipitating electrons of energy >43, >114, and >292 keV in the Northern Hemisphere (NH). Babu et al. (2022) defines the equatorward boundary as the latitude at which the electron flux (as a function of latitude) crosses a background threshold with a positive gradient. A detailed explanation of this can be found in Section 3 of Babu et al. (2022). For >43 keV EEP, 80% of the equatorward boundaries predicted by the model are within $\pm2.2°$ CGM latitude over a full solar cycle (2004–2014).

Despite high accuracy, Babu et al. (2022)'s model suffered from a solar cycle bias. The model underestimates the equatorward boundary during the declining phase and overestimates the equatorward boundary during solar minimum years, causing a potential solar cycle bias of up to 3.35°CGM latitude. This systematic bias potentially arises because the quiet time baseline of the Dst index changes with time (Lühr & Maus, 2010; Olsen et al., 2005; Temerin & Li, 2015), which might hamper its use in long-term quantitative modeling. To address this challenge Olsen et al. (2014) introduced an alternative ring current (RC) index which has been shown to be a valuable alternative to Dst, as demonstrated for example, by Luehr et al. (2016).

Moreover, based on higher accuracy during High-speed Solar wind Streams (HSS)/Co-rotating Interaction Regions (CIRs), Babu et al. (2022) speculate that selecting the solar wind driver as a dependent variable can improve the accuracy of a geomagnetic index-based model. The population in the radiation belt is primarily a result of Coronal Mass Ejections ((CME), HSS)/CIRs, and slow solar winds permeating the near-Earth space (Borovsky & Denton, 2006). The different driver characteristics and the subsequent magnetospheric processes determine the intensity of the MEE and the extent of the precipitation region (Asikainen & Ruopsa, 2016; Shen et al., 2017; Tyssøy et al., 2019; Yuan & Zong, 2012). As the frequency of the solar wind drivers is known to vary over the solar cycle, they might provide a tool to explain and remove the systematic solar cycle bias.

Furthermore, Laundal et al. (2017) shows the Earth's magnetic field structure deviates significantly from the dipole alignment at ionospheric heights leading to hemispheric asymmetries in the magnetosphere-ionosphere-thermosphere coupling. This deviation implies hemispheric differences in atmospheric responses to MEE precipitation, suggesting a need to model them separately in both hemispheres.

This study is an update of Babu et al. (2022)'s model of the equatorial MEE boundary in the Northern Hemisphere (NH). The original model parameterized by pressure-corrected Dst (Dst*) is extended by including the RC index and the solar wind drivers as dependent variables. The main objective is to remove the above-mentioned systematic solar cycle bias to make it more adequate for use in climatological studies and quantitative modeling. We also extend the investigation to the Southern Hemisphere (SH) to adapt it for global use. The overarching objective is to provide a key element for constructing a realistic estimate of EEP variability to be applied in atmosphere climate models. Moreover, the model can also be applied to examine the importance of the location of the plasmapause in moderating wave-particle interactions that lead to precipitation and how the precipitation boundaries might relate to the inner edge of the outer radiation belts.

2. Data

2.1. MEPED Observation of MEE Precipitation

The MEPED instrument is a part of the Space Environment Monitor package onboard NOAA/POES and EUMETSAT/MetOp satellites that have been operational since 1978. Their sun-synchronous polar orbit at 800–850 km altitude with a stabilized spatial orientation (Evans & Greer, 2000) allows them to monitor trapped and precipitating particles near the foot of the field lines (Nesse Tyssøy et al., 2016; Rodger et al., 2010). The orbital period of each satellite is ~102 min, and each orbit covers similar MLT sectors in the process. The second-generation SEM-2 instrument used in this study has been operational since 1998, having measured protons and electrons for two full solar cycles at present. It measures protons and electrons over

a broad range of energies through 0° and 90° solid-state detectors. We use the electron detectors that cover three energy channels that count electrons having energies from 30 keV to ~1 MeV. This is done through their three integral electron flux measurement channels E1, E2, and E3 of nominal energy values >30, >100, and >300 keV (Evans & Greer, 2000). However, the detector's efficiency depends on the energy spectrum of the encountered electrons (Yando et al., 2011). Ødegaard et al. (2017) uses the simulated detector efficiency reported in Yando et al. (2011) to determine effective integral energy levels of >43, >114 and >292 keV and associated geometric factors, which we utilize. False proton counts are removed from the electron channels using the proton telescope (Nesse Tyssøy et al., 2016). The proton spectrum is adjusted for degradation due to radiation damage by applying correction factors derived by Sandanger et al. (2015) and Ødegaard et al. (2016).

The 0° MEPED telescope points toward the local zenith while the 90° telescope is aligned orthogonal to the 0° telescope and anti-parallel to the spacecraft velocity vector. The 0° telescope is optimal for measuring MEE precipitating toward the center of the atmospheric BLC, the pitch angle range of electrons which will be lost to the atmosphere, at L-shells greater than ~1.5, while the 90° telescope counts particles both inside and outside the atmospheric BLC (Evans & Greer, 2000; Meredith et al., 2011; Nesse Tyssøy et al., 2016; Rodger et al., 2010). Determining particles inside the atmospheric BLC presents a challenge since the 0° and 90° telescopes only observe parts of the pitch angle distribution. This causes the 0° and 90° telescopes to under- and overestimate precipitating MEE fluxes, respectively. Therefore, we use a combination of fluxes from 0° and 90° detectors alongside the theoretical Fokker-Planck solutions of pitch-angle distribution of electrons in the magnetosphere to obtain an estimate of BLC fluxes that precipitate. A detailed methodology of this calculation can be found in Nesse Tyssøy et al. (2016).

The Fokker-Planck solution is independent of the type of wave-particle interactions responsible for the pitch angle distribution (Kennel & Petschek, 1966). The limitation of this theoretical approach is related to the assumption that the pitch angle distribution is in diffusive equilibrium where the particles being lost will be replenished. (L. Y. Li et al., 2013) applying a similar approach, however, has shown that without any strict criteria, the diffusion coefficient estimated from the MEPED instrument was consistent with independent observations of chorus waves by the Van Allen Probes.

2.2. Solar Wind Structure Identification

For analysis of the equatorward MEE precipitation boundaries with respect to different solar wind structures, we use the list created by co-author I. G. Richardson. This list uses solar wind parameters, geomagnetic indices retrieved from the NASA OMNIweb database, and observations of cosmic rays with energies between ~0.1 and 1 GeV, to separate solar wind structures into three categories: CME-associated, HSS/CIR, and slow ambient solar wind. A detailed description can be found in Richardson and Cane (2012).

2.3. The RC Index Monitoring the Strength of the Magnetospheric Ring Current

The strength of the magnetospheric ring current is often described by the Dst index (e.g., Sugiura, 1964). However, the baseline of Dst is known to contain erroneous time variations and jumps (e.g., Kauristie et al., 2016; Lühr & Maus, 2010; Olsen et al., 2005; Temerin & Li, 2015) due to its determination in annual (or monthly) batches. This implies that a specific storm will have different Dst signatures dependent on when in the solar cycle it occurs. These errors hamper the use of Dst in climatological studies and quantitative modeling. Olsen et al. (2014) introduced an alternative index, called RC, which is derived via hour-by-hour spherical harmonic analysis of magnetic data from a number of (presently 14) worldwide distributed observatories at mid and low latitudes. RC was originally designed to account for the magnetospheric contributions during the geomagnetic quiet conditions used for deriving models of the Earth's main field. However, the index turned out to be a valuable alternative to Dst also during more disturbed conditions, as demonstrated for example, by Luehr et al. (2016).

Since details of its derivation have been modified since the introduction of RC by Olsen et al. (2014) we here provide a brief but complete description of its derivation.

Magnetic data from 14 geomagnetic observatories (IAGA observatory codes ASP, BOU, CLF, FRD, GUA, HER, HON, KAK, KOU, LRM, ASC, NGK, SJG, SPT) between −34° and +52° dipole latitude are used and processed as follows:

1. The time-dependent core field, as given by the CHAOS geomagnetic field model (Finlay et al., 2020), is subtracted from the hourly values of each vector component and each observatory;

2. An estimate of the large-scale outer magnetospheric field, that is, the non-ring current magnetospheric contribution as given by the CHAOS model, is subtracted (two different coordinate frames are used in CHAOS for modeling magnetospheric contributions: the Geocentric Solar Magnetospheric (GSM) coordinate frame is used for describing contributions from the tail and magnetopause, while the SM frame is used to model the magnetospheric ring-current; for deriving RC we only subtract the GSM-dependent part describing contributions from the outer magnetosphere);

3. The static magnetic field, due to contributions from Earth's crust, is estimated separately for each vector component and each observatory as the robust mean during geomagnetic quiet times (defined as Kp ≤ 2^0, |dDst/dt| ≤ 2 nT/hr) and subtracted from the data;

4. The horizontal vector components are rotated from the geodetic to the centered dipole coordinate frame using Equations 7–10 of Hulot et al. (2015);

5. For each hour a spherical harmonic scalar potential model (up to spherical harmonic degree 1, corresponding to three coefficients) is fitted to the horizontal vector component data from as many as possible of the selected 14 observatories. Only data between 18:00 and 08:00 local time (i.e., local night) are used in an effort to minimize the impact of ionospheric contributions (e.g., Sq), and thus the number of observatories changes from hour to hour. The spherical harmonic fit is carried out in dipole coordinates using a robust estimation scheme with Huber weights (Constable, 1988).

6. The RC index is defined to be the (negative) first expansion coefficient in a spherical harmonic expansion of the magnetic potential assuming external sources. The minus sign is introduced to make RC(t) compatible with the definition of Dst(t) as the southward component of the magnetic field at the dipole equator.

7. Since RC(t) is derived from the horizontal components only, it consists of the sum of the magnetic field due to external, magnetospheric, and internal, Earth-induced electric currents. In the final step RC(t) = RC$_E$(t) + RC$_I$(t) is decomposed into external and induced parts, respectively, using a model of electrical conductivity of the Earth's mantle, as described in the section "Treatment of induced fields" of Finlay et al. (2020).

In the following, we use $RC_E(t)$, the external part of the RC-index, as a measure of the strength of the magnetospheric ring current.

3. Resolving the Solar Cycle Bias for the Existing MEE Boundary Model in the Northern Hemisphere

The pressure-corrected Dst index,

$$\text{Dst}^* = \text{Dst} - \left(15.8 \times P^{0.5}\right) + 20, \tag{1}$$

removes the magnetopause current induced by solar wind dynamic pressure (P) from the Dst index (Burton et al., 1975). Babu et al. (2022) found Dst* to be the best predictor of the equatorward boundary of MEE precipitation in the NH, outperforming Kp, AE, Ap, Bz, By, Ey, solar wind flow pressure and solar wind flow speed (v) in their analysis (Figure 4 in Babu et al. (2022)).

However, the Dst*-based model by Babu et al. (2022) exhibits a systematic solar cycle bias resulting in an estimate error of up to 3.35° Corrected Geomagnetic Latitude (CGMLat). This bias was speculated to be a consequence of the variation of the quiet-time baseline of the Dst index (Temerin & Li, 2015). This quiet-time baseline variation results in Dst underestimating or overestimating the level of geomagnetic activity with respect to the variations in the solar cycle. Babu et al. (2022) also found days dominated by HSS/CIR had the smallest error compared to days with CME or days with ambient/slow solar wind. Since different solar wind structures dominate different phases of a solar cycle (Richardson et al., 2001), Babu et al. (2022) postulated this might contribute to the solar cycle bias.
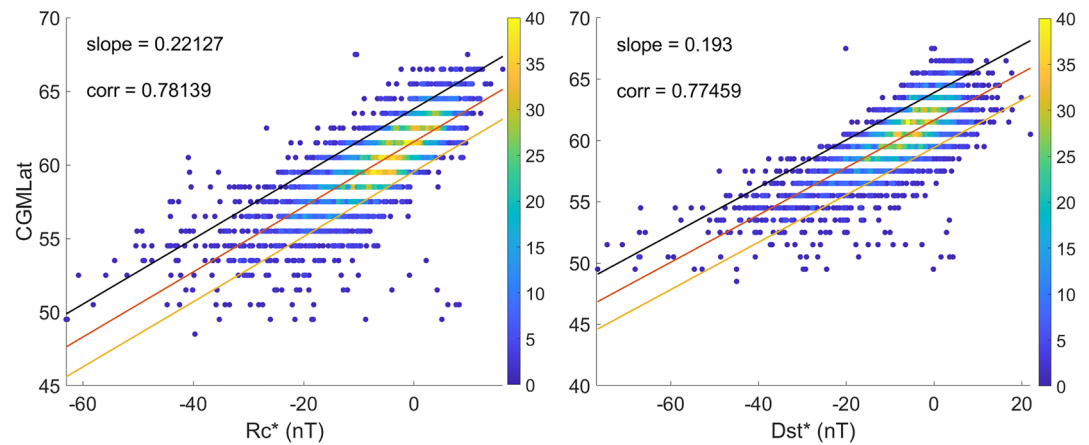
Figure 1. A comparison between the RC* index (left) and Dst* index (right). The red line is the linear fit. The yellow and the black lines are the 10th and the 90th percentiles of the residuals, respectively, when the boundaries predicted by each index are subtracted from the identified boundaries. The color bar represents the number density of data points. The data is from the E1 (>43 keV) energy channel in the 0–3 MLT sector.

After several unsuccessful attempts to correct the systematic solar cycle bias in the Dst* linear regression model, we became aware of the less-known RC index. The derivation of the RC index does not include a baseline correction. As illustrated in Figure 1, the pressure-corrected RC-index,

$$\mathrm{RC}^* = \mathrm{RC} - \left(15.8 \times P^{0.5}\right) + 20, \tag{2}$$

provides a marginally stronger linear dependence with the NH equatorial boundaries compared to the Dst*-based model with a correlation coefficient of 0.78 compared to 0.77. This supports the conclusion by Luehr et al. (2016) that the RC-index works well also during disturbed geomagnetic conditions.

Moreover, we find a multiple linear regression (MLR) model that includes both the Dst index and the RC index to be more accurate than a simple linear regression model that includes only one of these indices. By allowing for non-linear relationships in the model, the complex and dynamic nature of the magnetosphere can be captured to a greater extent. The use of interaction terms, polynomial terms, and correlated errors are also important in the model for a better fit and more accurate predictions. The MLR model is as follows,

$$\begin{aligned}
\text{Model Boundary } =\ & x_0 + (x_1 \times \mathrm{Dst}^*) + \left(x_2 \times \mathrm{RC}^*\right) + \\
& \left(x_3 \times (\mathrm{Dst}^*)^2\right) + \left(x_4 \times \left(\mathrm{RC}^*\right)^2\right) + \left(x_5 \times \mathrm{Dst}^* \times \mathrm{RC}^*\right),
\end{aligned} \tag{3}$$

As an estimate independent of solar wind structures, we perform MLR on the full data set. In addition, to assess the contribution of each type of solar wind structure to the solar cycle bias, we perform MLR individually for days dominated by CME, HSS/CIR, and ambient/slow solar wind structures.

The y-intercept is x_0, and the regression coefficients are x_1–x_5. The regression coefficients for the three energy channels and three solar wind structures are given in Table 1. To assess the performance of the MLR model, we calculate the model residual by subtracting the boundary predicted by the MLR model from each identified boundary (Equation 4). The procedure to identify the equatorward boundary has been described by Babu et al. (2022). It is essentially the same as the procedure followed for the boundary in the SH, which will be described in Section 4.1 of this paper. The residuals are shown in Figure 2. The first panel is a comparison of Dst* and RC* indices. The second panel represents the residual of the Dst* model from Babu et al. (2022). The third panel shows the residuals of the MLR model that is independent of solar wind structures. The residuals in the fourth panel depict the MLR model that is dependent on the solar wind structures.

$$\text{Residual} = \text{Identified Boundary} - \text{Model Boundary} \tag{4}$$

Figure 2 shows that the underestimation during the solar minimum has been resolved in the MLR model. Consequently, 90th percentile lines have narrowed in panels 3 and 4 compared to panel 2. The MLR model dependent

Table 1

y-Intercepts, Regression Coefficients, and Correlation Coefficients of the Three Energy Channels Used to Predict the Equatorward Boundaries of Medium-Energy Electrons Precipitation in the Northern Hemisphere

	x_0	x_1	x_2	x_3	x_4	x_5	R
E1 Channel							
CME	61.83	0.1145	0.1892	0.0005	0.0026	−0.0007	0.7638
HSS/CIR	61.78	0.1000	0.2137	−0.0017	0.0014	0.0033	0.7902
Slow Solar Wind	62.02	0.0645	0.1905	−0.0006	0.0032	−0.0009	0.7114
E2 Channel							
CME	60.75	0.0243	0.1915	−0.0002	0.0033	−0.0023	0.7421
HSS/CIR	60.67	0.0268	0.1876	−0.0005	0.0038	−0.0024	0.7777
Slow Solar Wind	60.66	0.0068	0.1786	0.0001	0.0039	−0.0031	0.6770
E3 Channel							
CME	59.64	−0.0321	0.1674	−0.0001	0.0031	−0.0023	0.6284
HSS/CIR	59.86	−0.0023	0.1578	0.0012	0.0039	−0.0036	0.6429
Slow Solar Wind	59.56	−0.0050	0.1542	0.0013	0.0036	−0.0031	0.5864

Note. Pearson correlation coefficients between RC* index and the identified boundaries are given by *R*.

on the solar wind structures in panel 4 slightly outperforms the MLR model independent of the solar wind structures. Overall, the error estimate has been reduced from approximately ±2.24° CGMLat in the Dst* model to 80 percent of the residuals lying within 1.80° CGMLat to −1.77° CGMLat in the solar wind structure dependent MLR model. Over some periods (e.g., 2010–2013) the residuals seem to exhibit somewhat sinusoidal trends. The source of these trends is unclear, as neither the MEPED flux data nor the Dst and RC indices, evince such trends.
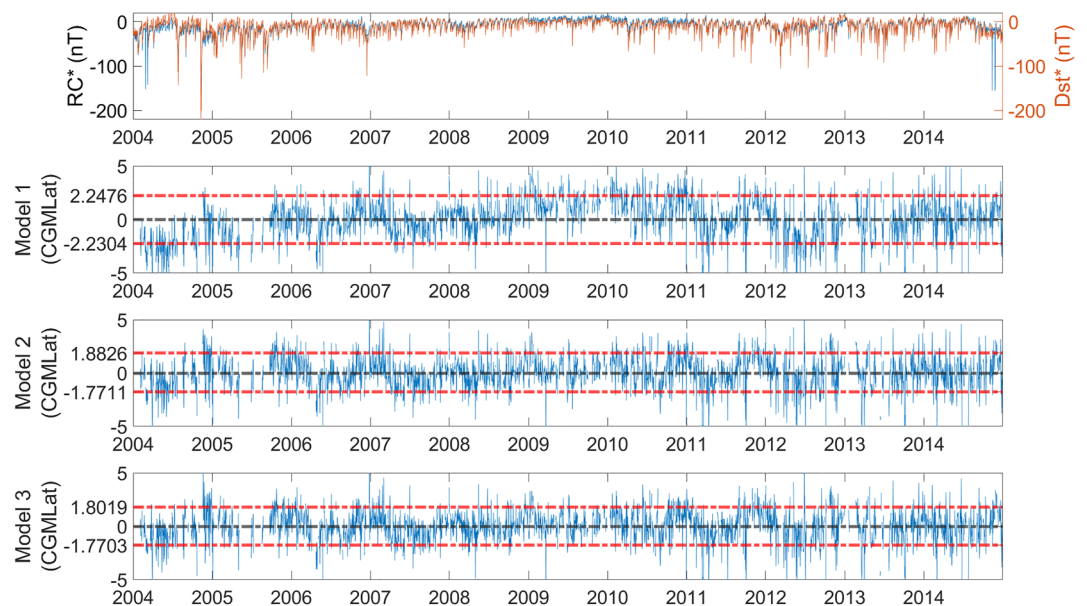

Figure 2. [first Panel] Rc* (blue) and Dst* (orange) during 2004–2014. [second Panel] Residual plot for the Dst* model. [third Panel] Residual plot for the multiple linear regression (MLR) model without solar wind structure separation. [fourth Panel] Residual plot for the MLR model with solar wind structure separation. The red dashed lines above and below the 0-line in the second, third, and fourth panels represent the 90th percentile values. The residuals are for the E1 energy channel.
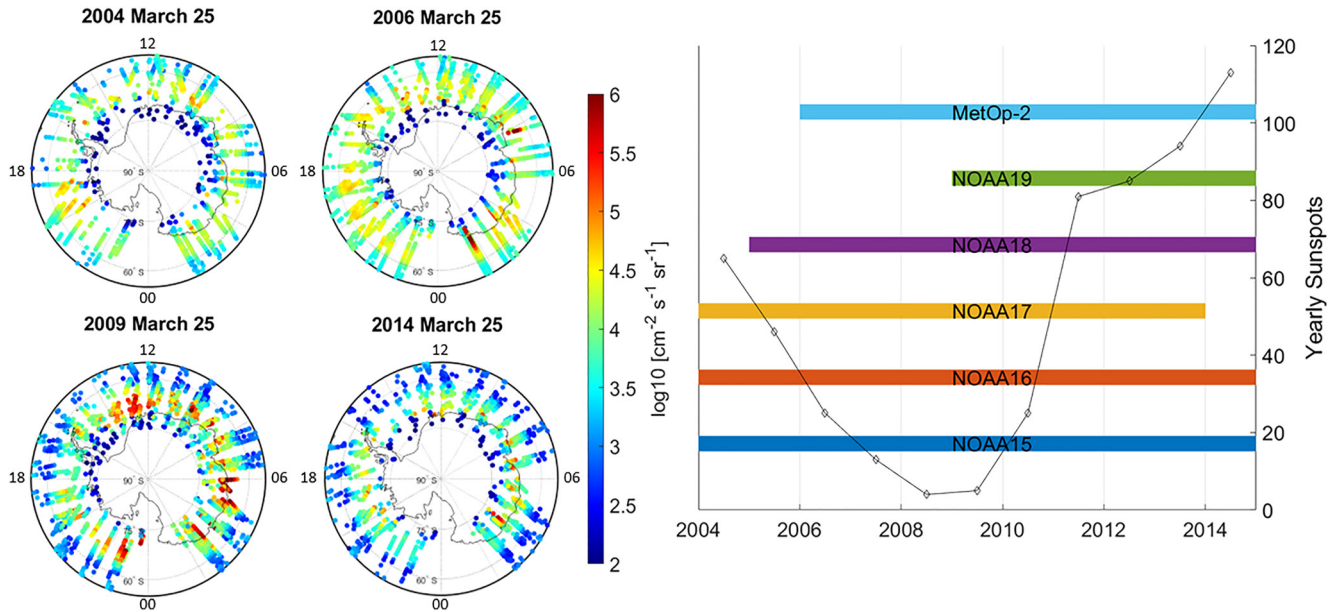
Figure 3. [Left] Daily electron flux observation (>43 keV) and satellite ground-track over the Southern Hemisphere on March 25 of 2004, 2006, 2009, and 2014. [Right] Polar Orbiting Environmental Satellites and MetOp satellite coverage during the 11 years of this study.

4. The Southern Hemisphere MEE Equatorial Boundary Model

The MEPED fluxes in the SH are obtained from six different satellites during 2004–2014: NOAA15, NOAA16, NOAA17, NOAA18, NOAA19, and MetOp2 as shown on the right half of Figure 3. The SH data between 90°W and 50°E geomagnetic longitude were removed in this study. This area corresponds to the South Atlantic Anomaly (SAA), a region of weak geomagnetic field causing high radiation close to the Earth's surface (Heirtzler, 2002; Vernov & Chudakov, 1960), resulting in constant high counts of precipitating particles in detectors onboard Low Earth Orbit satellites such as POES and MetOp (shown in Figure 4 of Rodger et al. (2013)). As seen in the left half of Figure 3, the satellites cover almost all MLT sectors. We take a daily average of electron fluxes and bin them into 180 latitudes and 8 MLT sectors resulting in a 1° CGMLat and 3-hr MLT resolution, respectively.
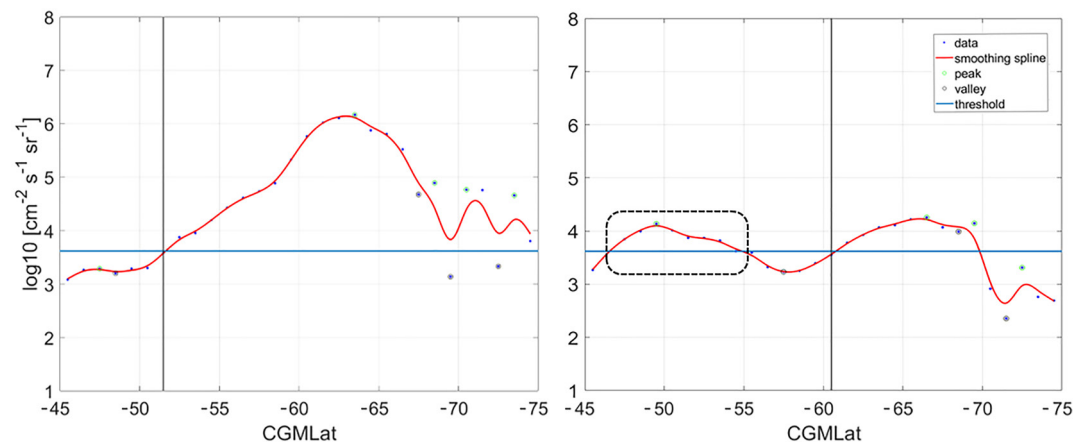
Figure 4. [Left] Sample electron flux observation (>43 keV) versus CGMLat with single peak over the threshold in the Southern Hemisphere. [Right] Same observation for a different day with a double peak over the threshold. The gray vertical lines are the equatorward boundaries identified by the algorithm. The black dashed box on the right panel represents the flux enhancement due to slot region filling events.
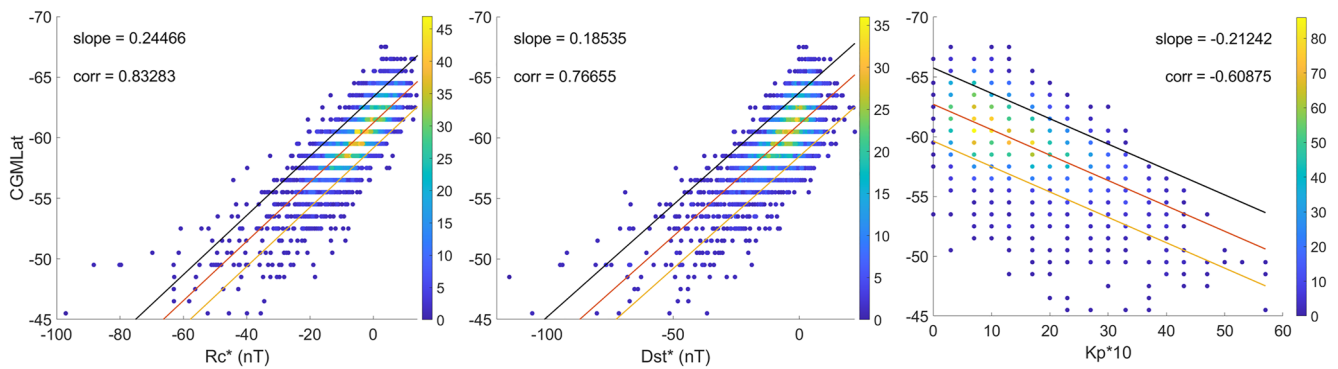
Figure 5. A comparison of the three best-correlated indices with the identified boundary in the Southern Hemisphere. [Left] RC*, [Center] Dst* and [Right] Kp. The red line is the linear fit. The yellow and the black lines are the 10th and the 90th percentiles of the residuals, respectively, when the boundaries predicted by each index are subtracted from the identified boundaries. The colorbar represents the number density of data points. The data is from the E1 (>43 keV) energy channel in the MLT sector 0–3.

4.1. Boundary Detection in the Southern Hemisphere

Identifying the equatorward boundary of precipitating MEE in the SH is implemented following the procedure described in Section 3 of Babu et al. (2022), which is as follows: We calculate a background threshold value for each energy channel independent of MLT sectors. This threshold is mean plus 2 standard deviations of fluxes in 50°–60° CGMLat range in the NH during days with slow/ambient solar wind conditions (blue horizontal line in Figure 4). Then we examine, at each day and each MLT zone, where the flux as a function of latitude crosses the threshold with a positive gradient within 45°–75° CGMLat. The point of this threshold crossing is identified as the equatorward boundary. Two examples of this procedure are illustrated separately in each panel of Figure 4, with the equatorward boundary indicated by the gray vertical line in each panel.

However, we face the challenge of enhanced fluxes at lower latitudes due to the filling of the slot region between the inner and outer radiation belts, identified by Kavanagh et al. (2018) as slot region filling events occurring during moderate to strong geomagnetic storm activity. The days in which slot region filling is observed are identified in Table A1 in the Appendix section. The fluxes associated with these events show a slow decay that lasts for a few weeks independent of any geomagnetic index or solar wind parameter. Therefore, they do not represent the dynamic MEE region we investigate and are discarded from this study. They represent 16% of the total days during 2004–2014 in the SH.

4.2. Linear Regression and MLR Model

In the SH, the RC* index outperforms Dst*, Kp, AE, Ap, Bz, By, Ey, P, and v with a Pearson correlation coefficient of 0.83 indicating that the RC* index has more predictive power in the SH compared to the NH. A comparison of the predictive capabilities of RC*, Dst*, and Kp indices are shown in Figure 5. The same MLR analysis described by Equation 3 in Section 3 is performed here to obtain the equatorward boundaries in the SH. The y-intercepts, regression coefficients, and Pearson correlation coefficients are given in Table 2.

As in the NH, the SH shows almost no difference in the median/mean value of precipitation boundaries across different MLT sectors. This suggests the >43 keV electrons, on average, complete multiple revolutions around the Earth per day before precipitating into the Earth's atmosphere. Although the MLR model gives higher correlation coefficients for the E1 channel in the SH, the residuals for the SH have a higher spread than in the NH, as seen in Figure 6. The reason for this is unclear, possibly associated with fewer data points associated with the removal of the SAA.

Similar to the NH residuals, the SH residuals exhibit an apparent sinusoidal trend. This apparent cyclic over- and underestimation are in phase at the two hemispheres which rules out potential seasonal biases in the MEPED flux data and/or the geomagnetic index parameters. Moreover, frequency analysis of the equatorial boundaries, the Dst*, and RC* indices do not explain these features.

Table 2
y-Intercepts, Regression Coefficients, and Correlation Coefficients of the Three Energy Channels Used to Predict the Southern Hemisphere Equatorward Boundary of Medium-Energy Electrons Precipitation

|	$x0$	$x1$	$x2$	$x3$	$x4$	$x5$	R
E1 Channel							
CME	−61.41	−0.0894	−0.2054	0	−0.0010	−0.0006	−0.8332
HSS/CIR	−61.30	−0.0925	−0.2183	−0.0002	−0.0009	−0.0005	−0.8367
Slow Solar Wind	−61.59	−0.0263	−0.2337	0.0007	−0.0014	−0.0003	−0.7696
E2 Channel							
CME	−60.29	−0.0196	−0.2556	0.0004	−0.0015	−0.0001	−0.7733
HSS/CIR	−60.23	−0.0299	−0.2007	−0.0010	−0.0026	0.0034	−0.7819
Slow Solar Wind	−60.03	0.0179	−0.2083	0	−0.0022	0.0015	−0.6512
E3 Channel							
CME	−58.98	0.0364	−0.1400	0.0009	0.0004	−0.0011	−0.7493
HSS/CIR	−59.21	0.0334	−0.1557	−0.0008	−0.0026	0.0035	−0.6551
Slow Solar Wind	−58.97	0.0329	−0.1819	−0.0010	−0.0037	0.0026	−0.5887

Note. Pearson correlation coefficients between RC* index and the identified boundaries are given by *R*.

5. Discussion

Past studies modeling the equatorward boundary of >30 keV electron precipitation such as van de Kamp et al. (2016) and van de Kamp et al. (2018) have used O'Brien and Moldwin (2003)'s plasmapause model, which depends on the Ap-index. Chorus waves are an important driver of MEE precipitation in the vicinity of the plasmapause (Lam et al., 2010; H. Li et al., 2016; Horne et al., 2005). We find O'Brien and Moldwin (2003)'s plasmapause location and the MLR model boundary have similar geomagnetic latitudes under quiet conditions, as seen in Figure 7. As the level of geomagnetic activity increases, however, the two models diverge for both hemispheres. A similar observation was made by Babu et al. (2022), whose Dst*-based model of the NH equatorward boundary also shows large discrepancies with the plasmapause model during days dominated by CMEs and HSS/CIRs.
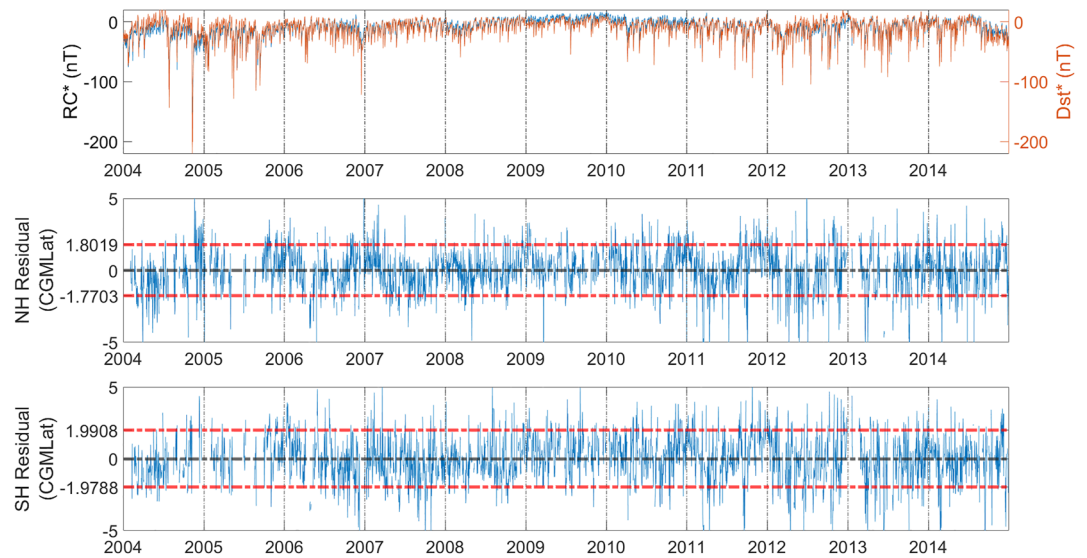
Figure 6. [first Panel] RC* (black) and Dst* (red) from 2004 to 2014. [second Panel] Residual plot for the Northern Hemisphere. [third Panel] Residual plot for the Southern Hemisphere. The red dashed lines above and below the 0-line in the second and third panels represent the 90th percentile values. The residuals are for the E1 energy channel.
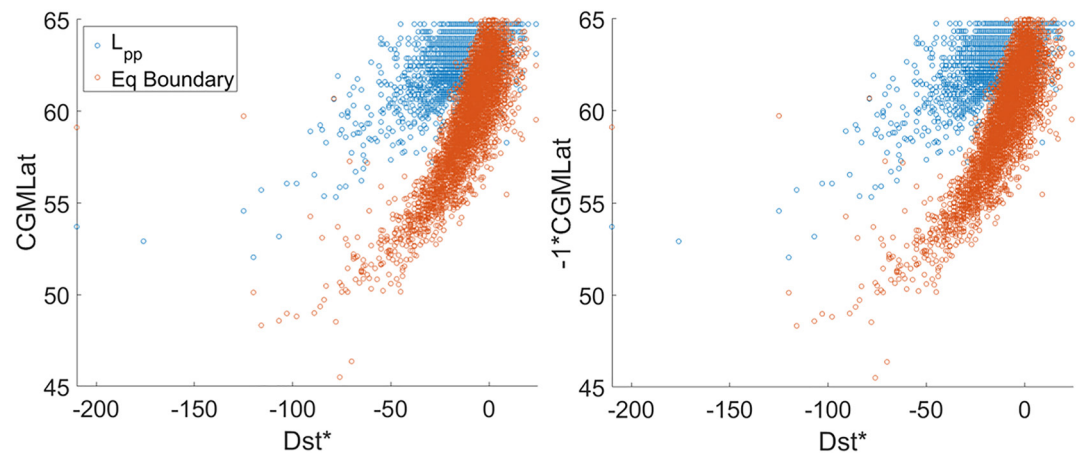
Figure 7. A comparison of equatorward boundaries predicted by the multiple linear regression (MLR) model and the O'Brien and Moldwin (2003) plasmapause model in the Northern (left) and Southern (right) Hemispheres. L_{pp} is the location of the plasmapause represented by the blue circles and the equatorward boundary from the MLR model is represented by the red circles. The data are from the E1 energy channel in the MLT sector 0–3.

In the High Energy Particle Precipitation in the Atmosphere (HEPPA) III-based intercomparison study of different atmospheric ionization rate models due to MEE precipitation, Nesse Tyssøy et al. (2022) found that the van de Kamp et al. (2016) model estimates a narrower extent of the precipitation region compared to the other MEE estimates, including the BLC flux used in this study. This finding suggests that differences in the hemispheric energy deposition of MEEs are not solely attributed to variations in the intensity and duration of MEE events, but also to the underestimation of the spatial extent of MEE precipitation (Nesse Tyssøy et al., 2022). van de Kamp et al. (2016) is part of the solar input recommendation for the chemistry-climate models such as the Coupled Model Intercomparison Project Phase 6 (CMIP6). Therefore, if implemented in atmospheric chemistry-climate models, our MLR model will have a higher chemical impact due to its relatively larger spatial extent both in the Northern and the Southern Hemispheres. Additionally, Laundal et al. (2017) and Kilifarska (2017) show that interhemispheric asymmetries affect the magnetosphere-ionosphere-thermosphere coupling and atmospheric response to particle precipitation. Hence, mutually independent models of the equatorward boundary for the Northern and Southern Hemispheres could increase the accuracy of global climate models.

The MLR model might also be applied to examine the importance of the location of the plasmapause in moderating wave-particle interactions that lead to precipitation. This examination would be based on periods where the precipitation boundary is well defined, ignoring periods where the identification of the boundaries may be influenced by slot region filling events. The MEE precipitation associated with the slot region filling events shows a slow decay that lasts for days independent of the geomagnetic activity level. Furthermore, applying the MLR model specifically during the slot region filling events can be useful to identify whether the MEE precipitation is mainly driven by factors such as chorus waves outside of the plasmasphere, or alternatively, by plasmaspheric hiss and whistler waves.

6. Conclusion

A more accurate geomagnetic index-based model that predicts the equatorward extent of Medium Energy Electron (MEE) precipitation is obtained through a MLR model of RC* and Dst* indices. The model is developed from BLC estimates based on the MEPED instruments onboard the NOAA/POES and EUMETSAT/MetOp satellites from 2004 to 2014. This study resolved the systematic solar cycle bias observed in Babu et al. (2022)'s Dst* model through the incorporation of the RC* index. The MLR model is extended to the SH to address inter-hemispheric asymmetries in the atmospheric response to MEE precipitation. The MLR model, dependent on whether the near-Earth space is dominated by CME, HSS/CIR, or ambient/slow solar winds, slightly outperformed the MLR model independent of the solar wind structures. The solar wind-dependent MLR model can predict the equatorward boundaries in both the NH and SH in the geomagnetic latitude zone between ±45° and

±75° for precipitating electrons >43, >114, and >292 keV for all MLT sectors. In both the NH and SH, RC* gives the best correlation with identified boundaries, followed by Dst*, Kp, and AE, respectively.

Appendix A: List of Days With Ambiguous Boundaries in SH

Table A1 represents days with ambiguous boundaries detected in SH. They do not represent the dynamic MEE region and are discarded from this study.

Table A1
Day of Year (DOY) With Ambiguous Boundaries Following the Slot Region Filling Events

2004	2005	2006	2007	2008	2010	2011	2012	2013	2014
1–37	1–32	27	2–6	7	95–96	46	15	146–159	71
42–49	38–41	78–81	18	33	99–105	61	59	166	230
60–62	50–54	97–114	30–31	61	124–127	78	71–80	170	244
70–81	57	118	46	70–76	151–155	156	117–120	181–201	295–298
88–90	65–74	124–129	113	87–90	216–219	159	145	228	301
94–103	78	132–133	120–121	99–100		190	158	240	343–344
115	96–110	158–161	147–149	115		219–222	164	278–281	357–358
122	120–123	176	219	120		244	169	288	363
128–129	130–180	205	277	123–125		271–274	184–186		
133–136	190–229	209	323	127		299–304	193–197		
153	238–270	232–240	327–329	133			200–203		
167	281–283	247		218			233		
191	308–311	261–262					251		
199–200	346	267					277–280		
205–227	362	342–362					284–286		
230–236							291–294		
245–252							329–330		
258–268									
278									
288–290									
295									
299									
313–343									
348–353									
356–358									
364–366									

Note. They account for 16% of the total number of days examined in this study.

Data Availability Statement

The NOAA/POES MEPED data used in this study are available from the National Oceanic and Atmospheric Administration https://www.ngdc.noaa.gov/stp/satellite/poes/dataaccess.html. The MLT and CGMLat sorted MEPED data is available at Zenodo via https://doi.org/10.5281/zenodo.6590387 (Babu, 2022). Geomagnetic indices and solar wind parameters were obtained from NASA Omniweb at https://omniweb.gsfc.nasa.gov/form/dx1.html. RC index is available at https://github.com/ancklo/ChaosMagPy/tree/master/chaosmagpy/lib.

References

Andersson, M. E., Verronen, P. T., Wang, S., Rodger, C. J., Clilverd, M. A., & Carson, B. R. (2012). Precipitating radiation belt electrons and enhancements of mesospheric hydroxyl during 2004-2009. *Blackwell Publishing Ltd*, *117*(9). https://doi.org/10.1029/2011JD017246

Asikainen, T., & Ruopsa, M. (2016). Solar wind drivers of energetic electron precipitation. *Journal of Geophysical Research: Space Physics*, *121*(3), 2209–2225. https://doi.org/10.1002/2015JA022215

Babu, E. M. (2022). Determining latitudinal extent of energetic electron precipitation using MEPED on-board NOAA/POES [Dataset]. Zenodo. https://doi.org/10.5281/zenodo.6590387

Babu, E. M., Tyssøy, H. N., Smith-Johnsen, C., Maliniemi, V., Salice, J. A., Millan, R. M., & Richardson, I. G. (2022). Determining latitudinal extent of energetic electron precipitation using MEPED On-Board NOAA/POES. *Journal of Geophysical Research: Space Physics*, *127*(9), e2022JA030489. https://doi.org/10.1029/2022ja030489

Baumgaertner, A. J., Seppälä, A., Jöckel, P., & Clilverd, M. A. (2011). Geomagnetic activity related NOx enhancements and polar surface air temperature variability in a chemistry climate model: Modulation of the NAM index. *Atmospheric Chemistry and Physics*, *11*(9), 4521–4531. https://doi.org/10.5194/acp-11-4521-2011

Borovsky, J. E., & Denton, M. H. (2006). Differences between CME-driven storms and CIR-driven storms. *Journal of Geophysical Research*, *111*(A7), A07S08. https://doi.org/10.1029/2005JA011447

Burton, R., McPherron, R., & Russell, C. (1975). An empirical relationship between interplanetary conditions and Dst. *Journal of Geophysical Research*, *80*(31), 4204–4214. https://doi.org/10.1029/JA080i031p04204

Constable, C. G. (1988). Parameter estimation in non-Gaussian noise. *Geophysical Journal*, *94*(1), 131–142. https://doi.org/10.1111/j.1365-246x.1988.tb03433.x

Damiani, A., Funke, B., López-Puertas, M., Santee, M. L., Cordero, R. R., & Watanabe, S. (2016). Energetic particle precipitation: A major driver of the ozone budget in the Antarctic upper stratosphere. *Geophysical Research Letters*, *43*(7), 3554–3562. https://doi.org/10.1002/2016GL068279

Evans, D., & Greer, M. (2000). *Polar orbiting environmental satellite space environment monitor-2: Instrument description and archive data documentation*. U.S. Department of Commerce, National Oceanic and Atmospheric Administration, Oceanic and Atmospheric Research Laboratories, Space Environment Center. [For sale by the National Technical Information Service], [2000].

Fang, X., Randall, C. E., Lummerzheim, D., Solomon, S. C., Mills, M. J., Marsh, D. R., et al. (2008). Electron impact ionization: A new parameterization for 100 eV to 1 MeV electrons. *Journal of Geophysical Research*, *113*(9), A09311. https://doi.org/10.1029/2008JA013384

Finlay, C. C., Kloss, C., Olsen, N., Hammer, M. D., Tøffner-Clausen, L., Grayver, A., & Kuvshinov, A. (2020). The CHAOS-7 geomagnetic field model and observed changes in the South Atlantic Anomaly. *Earth Planets and Space*, *72*(1), 156. https://doi.org/10.1186/s40623-020-01252-9

Heirtzler, J. R. (2002). *The future of the South Atlantic anomaly and implications for radiation damage in space* Tech. Rep (Vol. 64). Retrieved from www.elsevier.com/locate/jastp

Horne, R. B., Thorne, R. M., Glauert, S. A., Albert, J. M., Meredith, N. P., & Anderson, R. R. (2005). Timescale for radiation belt electron acceleration by whistler mode chorus waves. *Journal of Geophysical Research*, *110*(A3), A03225. https://doi.org/10.1029/2004JA010811

Hulot, G., Sabaka, T., Olsen, N., & Fournier, A. (2015). The present and future geomagnetic field. In G. Schubert (Ed.), *Treatise on geophysics* (2nd ed., Vol. 5, pp. 33–78). Elsevier. https://doi.org/10.1016/B978-0-444-53802-4.00096-8

Kauristie, K., Morschhauser, A., Olsen, N., Finlay, C. C., McPherron, R. L., Gjerloev, J. W., & Opgenoorth, H. J. (2016). On the usage of geomagnetic indices for data selection in internal field modelling. *Space Science Reviews*, *206*(1–4), 61–90. https://doi.org/10.1007/s11214-016-0301-0

Kavanagh, A. J., Cobbett, N., & Kirsch, P. (2018). Radiation belt slot region filling events: Sustained energetic precipitation into the mesosphere. *Journal of Geophysical Research: Space Physics*, *123*(9), 7999–8020. https://doi.org/10.1029/2018JA025890

Kennel, C. F., & Petschek, H. E. (1966). *Limit on stably trapped particle fluxes* Tech. Rep. (Vol. 71).

Kilifarska, N. A. (2017). Hemispherical asymmetry of the lower stratospheric O_3 response to galactic cosmic rays forcing. *ACS Earth and Space Chemistry*, *1*(2), 80–88. https://doi.org/10.1021/acsearthspacechem.6b00009

Lam, M. M., Horne, R. B., Meredith, N. P., Glauert, S. A., Moffat-Griffin, T., & Green, J. C. (2010). Origin of energetic electron precipitation >30 KeV into the atmosphere. *Journal of Geophysical Research*, *115*(A4), A00F08. https://doi.org/10.1029/2009JA014619

Laundal, K. M., Cnossen, I., Milan, S. E., Haaland, S. E., Coxon, J., Pedatella, N. M., et al. (2017). North–South asymmetries in Earth's magnetic field. *Space Science Reviews*, *206*(1–4), 225–257. https://doi.org/10.1007/s11214-016-0273-0

Li, H., Yuan, Z., Wang, D., Huang, S., Qiao, Z., & Yu, X. (2016). Statistical characteristics of potentially chorus-driven energetic electron precipitation from POES observations. *Journal of Geophysical Research: Space Physics*, *121*(10), 9531–9546. https://doi.org/10.1002/2016JA023101

Li, L. Y., Yu, J., Cao, J. B., Zhang, D., Wei, X. H., Rong, Z. J., et al. (2013). Rapid loss of the plasma sheet energetic electrons associated with the growth of whistler mode waves inside the bursty bulk flows. *Journal of Geophysical Research: Space Physics*, *118*(11), 7200–7210. https://doi.org/10.1002/2013JA019109

Luehr, H., Xiong, C., Olsen, N., & Le, G. (2016). Near-earth magnetic field effects of large-scale magnetospheric currents. *Space Science Reviews*, *206*, 521–545. https://doi.org/10.1007/s11214-016-0267-y

Lühr, H., & Maus, S. (2010). Solar cycle dependence of magnetospheric currents and a model of their near-Earth magnetic field. *Earth Planets and Space*, *62*(10), 843–848. https://doi.org/10.5047/eps.2010.07.012

Maliniemi, V., Asikainen, T., Salminen, A., & Mursula, K. (2019). Assessing North Atlantic winter climate response to geomagnetic activity and solar irradiance variability. *Quarterly Journal of the Royal Meteorological Society*, *145*(725), 3780–3789. https://doi.org/10.1002/qj.3657

Maliniemi, V., Nesse Tyssøy, H., Smith-Johnsen, C., Arsenovic, P., & Marsh, D. R. (2021). Effects of enhanced downwelling of NOx on Antarctic upper-stratospheric ozone in the 21st century. *Atmospheric Chemistry and Physics*, *21*(14), 11041–11052. https://doi.org/10.5194/acp-21-11041-2021

Matthes, K., Funke, B., Andersson, M. E., Barnard, L., Beer, J., Charbonneau, P., et al. (2017). Solar forcing for CMIP6 (v3.2). *Geoscientific Model Development*, *10*(6), 2247–2302. https://doi.org/10.5194/gmd-10-2247-2017

Meredith, N. P., Horne, R. B., Lam, M. M., Denton, M. H., Borovsky, J. E., & Green, J. C. (2011). Energetic electron precipitation during high-speed solar wind stream driven storms. *Journal of Geophysical Research*, *116*(5), A05223. https://doi.org/10.1029/2010JA016293

Nesse Tyssøy, H., Sandanger, M. I., Ødegaard, L. K., Stadsnes, J., Aasnes, A., & Zawedde, A. E. (2016). Energetic electron precipitation into the middle atmosphere—Constructing the loss cone fluxes from MEPED POES. *Journal of Geophysical Research A: Space Physics*, *121*(6), 5693–5707. https://doi.org/10.1002/2016JA022752

Nesse Tyssøy, H., Sinnhuber, M., Asikainen, T., Bender, S., Clilverd, M. A., Funke, B., et al. (2022). HEPPA III intercomparison experiment on electron precipitation impacts: 1. Estimated ionization rates during a geomagnetic active period in April 2010. *Journal of Geophysical Research: Space Physics*, *127*(1), e2021JA029128. https://doi.org/10.1029/2021JA029128

O'Brien, T. P., & Moldwin, M. B. (2003). Empirical plasmapause models from magnetic indices. *Geophysical Research Letters*, *30*(4), 1152. https://doi.org/10.1029/2002GL016007

Ødegaard, L.-K. G., Nesse, T. H., Sandanger, M. I. J., Stadsnes, J., & Søraas, F. (2016). Space weather impact on the degradation of NOAA POES MEPED proton detectors. *Journal of Space Weather and Space Climate*, *6*, A26. https://doi.org/10.1051/swsc/2016020

Ødegaard, L.-K. G., Nesse, T. H., Søraas, F., Stadsnes, J., & Sandanger, M. I. (2017). Energetic electron precipitation in weak to moderate corotating interaction region-driven storms. *Journal of Geophysical Research: Space Physics*, *122*(3), 2900–2921. https://doi.org/10.1002/2016JA023096

Olsen, N., Lühr, H., Finlay, C. C., Sabaka, T. J., Michaelis, I, Rauberg, J., & Tøffner-Clausen, L. (2014). The CHAOS-4 geomagnetic field model. *Geophysical Journal International*, *197*(2), 815–827. https://doi.org/10.1093/gji/ggu033

Olsen, N., Sabaka, T. J., & Lowes, F. (2005). New parameterization of external and induced fields in geomagnetic field modeling, and a candidate model for IGRF 2005. *Earth Planets and Space*, *57*(12), 1141–1149. https://doi.org/10.1186/bf03351897

Richardson, I. G., & Cane, H. V. (2012). Near-Earth solar wind flows and related geomagnetic activity during more than four solar cycles (1963–2011). *Journal of Space Weather and Space Climate*, *2*, A02. https://doi.org/10.1051/swsc/2012003

Richardson, I. G., Cliver, E. W., & Cane, H. V. (2001). Sources of geomagnetic storms for solar minimum and maximum conditions during 1972–2000. *Geophysical Research Letters*, *28*(13), 2569–2572. https://doi.org/10.1029/2001GL013052

Rodger, C. J., Clilverd, M. A., Green, J. C., & Lam, M. M. (2010). Use of POES SEM-2 observations to examine radiation belt dynamics and energetic electron precipitation into the atmosphere. *Journal of Geophysical Research*, *115*(4), A04202. https://doi.org/10.1029/2008JA014023

Rodger, C. J., Kavanagh, A. J., Clilverd, M. A., & Marple, S. R. (2013). Comparison between POES energetic electron precipitation observations and riometer absorptions: Implications for determining true precipitation fluxes. *Journal of Geophysical Research: Space Physics*, *118*(12), 7810–7821. https://doi.org/10.1002/2013JA019439

Sandanger, M., Ødegaard, L., Hn, T., Stadsnes, J., Søraas, F., Oksavik, K., & Aarsnes, K. (2015). In-flight calibration of NOAA POES proton detectors—Derivation of the MEPED correction factors. *Journal of Geophysical Research: Space Physics*, *120*(11), 9578–9593. https://doi.org/10.1002/2015JA021388

Seppälä, A., Randall, C., Clilverd, M., Rozanov, E., & Rodger, C. (2009). Geomagnetic activity and polar surface air temperature variability. *Journal of Geophysical Research*, *114*(A10), A10312. https://doi.org/10.1029/2008JA014029

Shen, X.-C., Hudson, M. K., Jaynes, A. N., Shi, Q., Tian, A., Claudepierre, S. G., et al. (2017). Statistical study of the storm time radiation belt evolution during Van Allen Probes era: CME-versus CIR-driven storms. *Journal of Geophysical Research: Space Physics*, *122*(8), 8327–8339. https://doi.org/10.1002/2017JA024100

Sinnhuber, M., Nieder, H., & Wieters, N. (2012). Energetic particle precipitation and the chemistry of the mesosphere/lower thermosphere. *Surveys in Geophysics*, *33*(6), 1281–1334. https://doi.org/10.1007/s10712-012-9201-3

Solomon, S., Crutzen, P. J., & Roble, R. G. (1982). Photochemical coupling between the thermosphere and the lower atmosphere: 1. Odd nitrogen from 50 to 120 km. *Journal of Geophysical Research*, *87*(C9), 7206–7220. https://doi.org/10.1029/JC087iC09p07206

Sugiura, M. (1964). Hourly values of equatorial Dst for IGY. *Annals of the International Geophysical Year*, *35*, 49.

Temerin, M., & Li, X. (2015). The Dst index underestimates the solar cycle variation of geomagnetic activity. *Journal of Geophysical Research: Space Physics*, *120*(7), 5603–5607. https://doi.org/10.1002/2015JA021467

Turunen, E., Verronen, P. T., Seppälä, A., Rodger, C. J., Clilverd, M. A., Tamminen, J., et al. (2009). Impact of different energies of precipitating particles on NOx generation in the middle and upper atmosphere during geomagnetic storms. *Journal of Atmospheric and Solar-Terrestrial Physics*, *71*(10–11), 1176–1189. https://doi.org/10.1016/j.jastp.2008.07.005

Tyssøy, H. N., Haderlein, A., Sandanger, M., & Stadsnes, J. (2019). Intercomparison of the POES/MEPED loss cone electron fluxes with the CMIP6 parametrization. *Journal of Geophysical Research: Space Physics*, *124*(1), 628–642. https://doi.org/10.1029/2018JA025745

van de Kamp, M., Rodger, C. J., Seppälä, A., Clilverd, M. A., & Verronen, P. T. (2018). An updated model providing long-term data sets of energetic electron precipitation, including zonal dependence. *Journal of Geophysical Research: Atmospheres*, *123*(17), 9891–9915. https://doi.org/10.1029/2017JD028253

van de Kamp, M., Seppälä, A., Clilverd, M. A., Rodger, C. J., Verronen, P. T., & Whittaker, I. C. (2016). A model providing long-term data sets of energetic electron precipitation during geomagnetic storms. *Journal of Geophysical Research: Atmospheres*, *121*(20), 12520–12540. https://doi.org/10.1002/2015JD024212

Vernov, S., & Chudakov, A. (1960). Terrestrial corpuscular radiation and cosmic rays. *Space Research*, 751.

Verronen, P. T., Rodger, C. J., Clilverd, M. A., & Wang, S. (2011). First evidence of mesospheric hydroxyl response to electron precipitation from the radiation belts. *Journal of Geophysical Research*, *116*(7), D07307. https://doi.org/10.1029/2010JD014965

Yando, K., Millan, R. M., Green, J. C., & Evans, D. S. (2011). A Monte Carlo simulation of the NOAA POES medium energy proton and electron detector instrument. *Journal of Geophysical Research*, *116*(A10), A10231. https://doi.org/10.1029/2011JA016671

Yuan, C. J., & Zong, Q.-G. (2012). Quantitative aspects of variations of 1.5–6.0 MeV electrons in the outer radiation belt during magnetic storms. *Journal of Geophysical Research*, *117*(A11), A11208. https://doi.org/10.1029/2011JA017346

Zawedde, A. E., Nesse Tyssøy, H., Stadsnes, J., & Sandanger, M. I. (2019). Are EEP events important for the tertiary ozone maximum? *Journal of Geophysical Research: Space Physics*, *124*(7), 5976–5994. https://doi.org/10.1029/2018JA026201

Zúñiga López, H. D., Tyssøy, H. N., Smith-Johnsen, C., & Maliniemi, V. (2022). The direct effect of medium energy electron precipitation on mesospheric dynamics during a sudden stratospheric warming event in 2010. *Geophysical Research Letters*, *49*(13), e2022GL097812. https://doi.org/10.1029/2022GL097812